CLM-P794

CLM-P794

UKAEA

Preprint

FINITE-ß EFFECTS ON TEARING MODES IN THE TOKAMAK

T. C. HENDER
R. J. HASTIE
D. C. ROBINSON

CULHAM LABORATORY
Abingdon, Oxfordshire
1987

CLM-P794

FINITE-ß EFFECTS ON TEARING MODES IN THE TOKAMAK

T C Hender, R J Hastie and D C Robinson

UKAEA/Euratom Association, Culham Laboratory, Abingdon, Oxon, OX14 3DB, UK

Abstract

Details are given of a numerical study of finite-β tearing modes in the Tokamak. The linear compressible resistive MHD equations are solved in full toroidal geometry with no ordering assumptions. The results show a strong stabilising effect as β is increased, arising from the average curvature within the resistive layer. This stabilising effect is particularly pronounced for high conductivity temperatures and small aspect ratios.

(Submitted for publication in Nuclear Fusion)

October 1986

1 Introduction

The effects of plasma pressure on tearing modes in toroidal geometry were studied analytically by Glasser et al [1]. They found a strong stabilising effect at finite beta, resulting from the influence of the average curvature on the tearing mode within the resistive layer. At $\beta=0$ in the cylindrical limit the stability criterion for the tearing mode [2] is

$$\lim_{\varepsilon\to 0}\left[\frac{1}{b_r}\frac{db_r}{d_r}\right]_{r_s-\varepsilon}^{r_s+\varepsilon} \equiv \Delta' < 0 \qquad (1)$$

where b_r is the perturbed radial magnetic field and r_s is the resonant surface radius. In the large aspect ratio limit the results of Ref [1] yield the modified tearing mode stability criterion

$$\Delta' < 1.54\ (V_s/X_0)\ |D_R|^{5/6}\ (\equiv \Delta'_c) \qquad (2)$$

where expressions for D_R and V_s/X_0 are given in Ref. [1] (and also in Section 3 of this paper). It is assumed that the average curvature is stabilising ($D_R<0$) in deriving Eq. (2); for $D_R>0$ (as in the RFP) pressure driven interchange instabilities occur. In general in the Tokamak $D_R<0$ and thus the region of stability to tearing modes improves. To understand the regimes where this stabilising effect on the tearing mode are important it is useful to examine the scaling of Δ'_c with minor radius (a), major radius (R_0), conductivity temperature (T), and central beta (β_0)

$$\Delta'_c \propto (a^2 T^2 q^5 \beta_0^2 / R_0)^{1/3} \qquad (3)$$

thus lowering the aspect ratio (at constant a or R_0) raises Δ'_c and similarly raising T or β_0 increases Δ'_c. So in small aspect ratio, high temperature Tokamaks (eg JET) the stabilising effects of the favourable average curvature will be particularly pronounced. Several authors have used cylindrical estimates for Δ' to examine these improved tearing mode stability boundaries for a range of Tokamaks [3,4].

In this paper we present numerical studies of the effects of finite beta and aspect ratio on the linear tearing mode. We solve the compressible or incompressible resistive magneto-hydrodynamic (MHD) equations in full toroidal geometry with no ordering assumptions, using a modified version of the FAR code [5]. The studies presented here will focus on parameters broadly consistent with the JET device, although various other aspect ratios are examined. The results presented confirm the stabilising effect on the tearing mode resulting from the favourable average curvature.

The analytic treatment of Ref. [1] assumes that Δ' is a given quantity. In practice Δ' is a function of β and aspect ratio, and when there are several rational surfaces with the same toroidal mode number (n) and different poloidal mode numbers (m) present in the plasma, a coupled system of ordinary differential equations must be solved for the Δ' at each rational surface. Since in general the q-profiles in Tokamaks do encompass several rational surfaces, so also will most of the cases studies in this paper. We will however examine one large

aspect ratio case with a central q value of 1.1 and an edge value of 2.9. For this case we make a detailed comparison with the analytic theory. The effects of toroidicity and pressure for situations with toroidal couplings have been studied using the finite beta reduced Tokamak equations [6] in Refs. [7,8]. The $o(\varepsilon^3)$ reduced Tokamak equations however preclude any curvature stabilisation because the pressure perturbation is advanced by fluid convection alone and compressibility effects are ignored. By expanding to higher order $[o(\varepsilon^5)]$ the curvature stabilisation effects are incorporated whilst the fast magneto-sonic waves are still precluded [9].

In Section 2, the form of the resistive MHD equations which we solve numerically are discussed and also very brief details of the numerics are given. The large aspect ratio analytic theory is described in Section 3, the numerical results are presented in Section 4, and finally a summary and conclusions are given in Section 5.

2 Resistive MHD Equations and Numerics

In this section details will be given of the resistive MHD equations which are solved and the numerical methods used. The code used is a version of the FAR code [5] which has been modified to solve the compressible resistive MHD equations. Only brief details of the numerics will be given here.

The MHD equations are solved in a system of flux coordinates (ρ, θ, ξ) [10]. Here ρ is a flux surface label, θ is a generalised poloidal angle determined from a straight field line condition and ξ is the toroidal angle. A generalised minor radius which is used to

normalise all lengths is defined by $a=\sqrt{(R_0 \int R^{-2} dV/(2\pi)^2)}$. These flux coordinates are generated numerically from Grad-Shafranov equilibrium solutions [11] and thus no orderings are used in their evaluation.

We start from the linear resistive MHD equations

$$\frac{\partial \vec{B}}{\partial t} = \nabla \times (\vec{V} \times \vec{B} - \eta \nabla \times \vec{B}) \tag{4}$$

$$\rho_m \frac{\partial \vec{V}}{\partial t} = S^2 (\vec{J} \times \vec{B} - \nabla P) \tag{5}$$

$$\frac{\partial P}{\partial t} = -\vec{V}.\nabla P - \gamma P \nabla.\vec{V} \tag{6}$$

and

$$\nabla.\vec{B} = 0 \tag{7}$$

Here γ is the ratio of specific heats. We assume that $\rho_m=\rho_m(\rho)$ and for the calculations presented here ρ_m will be a constant. In eqns (4)-(7) all lengths are normalised to a, the resistivity, pressure and density are normalised to their values at the magnetic axis η_0, P_0, ρ_0, respectively; time is normalised to $\tau_R=a^2/\eta_0$; the magnetic field to B_0 its vacuum value at R_0; $S=\tau_R/\tau_{Hp}$ is the ratio of the resistive time to the poloidal Alfven transit time ($\tau_{HP}=R\sqrt{\rho_0/B_0}$).

From eqn. (7) we may write

$$\vec{B} = \nabla \times \vec{A} = \nabla\theta \times \nabla (\rho\chi) + \nabla\xi \times \nabla\phi \qquad (8)$$

where we have adopted the gauge $A_\rho = 0$. We adopt a similar form for the velocity

$$\vec{V} = \nabla\theta \times \nabla (\rho\Lambda) + \nabla\xi \times \nabla\phi + \nabla\iota \qquad (9)$$

which separates the incompressible and compressible parts of the perturbation. From Eqn. (4) we determine equations for the poloidal and toroidal flux functions, ϕ and χ, respectively

$$\frac{\partial\chi}{\partial t} = \frac{F}{R^2}\left(\frac{\partial}{\partial\xi} - \frac{1}{q}\frac{\partial}{\partial\theta}\right)\Lambda + F\nabla\rho\cdot\nabla\iota - \frac{F}{\rho}\frac{\partial}{\partial\theta}\left(\frac{1}{R^2}\right)\left[\frac{\rho\Lambda}{q} - \phi\right]$$

$$\frac{-1}{\rho}\frac{\partial\alpha}{\partial\theta} + \eta J_\theta \qquad (10)$$

$$\frac{\partial\psi}{\partial t} = \frac{F}{R^2}\left(\frac{\partial}{\partial\xi} - \frac{1}{q}\frac{\partial}{\partial\theta}\right)\phi + \frac{\rho F}{q}\nabla\rho\cdot\nabla\iota - \frac{\partial\alpha}{\partial\xi} + \eta J_\xi \qquad (11)$$

where F is the equilibrium toroidal magnetic field (B_ξ) and α is the electrostatic potential. An equation for α is determined from the gauge constraint $A_\rho = 0$

$$\frac{\partial\alpha}{\partial\rho} = \frac{\partial}{\partial\rho}\left(\frac{F}{R^2}\right)\phi - \frac{\partial}{\partial\rho}\left(\frac{F}{q\,R^2}\right)\rho\,\Lambda - F\nabla\theta\cdot\nabla\iota + \eta J_\rho - \frac{\rho F\varepsilon^2}{q\,R^2}\frac{\partial\iota}{\partial\xi} \qquad (12)$$

here $\varepsilon = (a/R_0)$ is the inverse aspect ratio. Explicit expressions in terms of ϕ and χ for the perturbed currents (J_ρ, J_θ, J_ξ), occurring in

Eqns (10)-(12) are given in Ref. [5]. To obtain equations for the poloidal and toroidal velocity stream functions, ϕ and Λ, we take the curl of Eq. (5) which annihilates the compressible terms ($\nabla\iota$). Defining the vorticity $\vec{U}=\nabla\times\vec{V}$ we find

$$\frac{1}{S^2}\frac{\partial U^{\theta}}{\partial t} = \rho\left(\left[\frac{\partial\chi}{\partial\xi} - \frac{1}{\rho}\frac{\partial\psi}{\partial\theta}\right]\frac{\partial}{\partial\rho} + \frac{1}{\rho}\frac{\partial\psi}{\partial\rho}\frac{\partial}{\partial\theta} - \frac{1}{\rho}\frac{\partial\rho\chi}{\partial\rho}\frac{\partial}{\partial\xi}\right)\left(\frac{J^{\theta}}{\rho}\right)$$

$$- R^2\rho\vec{J}.\nabla\left(\frac{1}{R^2\rho}\frac{\partial\psi}{\partial\rho}\right) \qquad (13)$$

and

$$\frac{\varepsilon^2}{S^2}\frac{\partial U}{\partial t} = \left(\left[\frac{\partial\chi}{\partial\xi} - \frac{1}{\rho}\frac{\partial\psi}{\partial\theta}\right]\frac{\partial}{\partial\rho} + \frac{1}{\rho}\frac{\partial\psi}{\partial\theta}\frac{\partial}{\partial\rho} - \frac{1}{\rho}\frac{\partial\rho\chi}{\partial\rho}\frac{\partial}{\partial\xi}\right) J^{\xi}$$

$$+ \vec{J}.\nabla\left(\frac{1}{\rho R^2}\frac{\partial\rho\chi}{\partial\rho}\right) \qquad (14)$$

An equation for the compressible velocity potential (ι) is found by applying the divergence operator to Eq. (5)

$$\frac{1}{S^2}\frac{\partial}{\partial t}(\nabla^2\iota) = \nabla.(\vec{J}\times\vec{B}) - \frac{\beta_o}{2\varepsilon^2}\nabla^2 P \qquad (15)$$

Numerically we solve the linearised version of Eqs. (13) to (15). Finally the equation for the perturbed pressure (P) is

$$\frac{\partial P}{\partial t} = -\left[\frac{1}{R^2}\left(\frac{\partial\Lambda}{\partial s} - \frac{1}{\rho}\frac{\partial\phi}{\partial\theta}\right) + \nabla\rho.\nabla\iota\right]\frac{dP_{eq}}{d\rho} - \gamma P_{eq}\nabla^2\iota \qquad (16)$$

Equations (10)-(16) are equivalent to the primitive compressible MHD equations [Eqs. (4)-(7)] and contain no ordering assumptions. By setting $\iota=0$ in these equations we obtain the incompressible MHD equations. The ability to solve either the fully compressible or incompressible equations is retained in our numerical implementation.

Equations (10)-(16) are solved using a modified version of the FAR code, of which full numerical details are given in Ref. [5]. A Fourier decomposition is used in the angular variables (θ,ξ) and finite differences in ρ. An implicit time centred scheme is used which gives very rapid convergence of the solution [5,12]. The boundary conditions at the origin are determined by regularity. At the wall we require the normal components of $\hat{\mathbf{V}}$ and $\hat{\mathbf{B}}$ are zero. The boundary condition on the velocity may be split because of a gauge invariance into separate requirements on the incompressible

$$\frac{\partial \Lambda}{\partial \xi} = \frac{1}{\rho}\frac{\partial \phi}{\partial \theta} \tag{17}$$

and compressible

$$g^{\rho\rho}\frac{\partial \iota}{\partial \rho} + \frac{g^{\rho\theta}}{\rho}\frac{\partial \iota}{\partial \theta} = 0 \tag{18}$$

parts of the velocity. Full details of the remaining boundary conditions and their numerical implementation are given in Ref. [5]. The majority of calculations presented in this paper are repeated with varying spatial resolutions to check for convergence. Some details of this are given in Section 4.

3 Large Aspect Ratio Analytic Theory

In this section we examine the stability to n=1 modes of a circular boundary case with an aspect ratio of 20 and $q=1.1(1+(\rho/0.617)^8)^{1/4}$, and compare the results with analytic theory. For this case q varies between 1.1 and 2.9 and thus only the m=2 mode is resonant. In the large aspect ratio limit the dispersion relation derived in Ref. [1], which is appropriate to this case, is

$$\Delta' = 2.12\ \omega^{5/4}\ \frac{V_s}{X_0 Q_0^{5/4}}\left[1 - \frac{\pi}{4}\frac{D_R}{\omega^{3/2}}\ Q_0^{3/2}\right] \tag{19}$$

where ω is normalised to τ_{HP},

$$\frac{V_s}{X_0 Q_0^{5/4}} = \left(\frac{\eta}{S}\right)^{-3/4}\ \left(\frac{nq'}{q}\right)^{-1/2}\ (1 + 2q^2)^{1/4} \tag{20}$$

$$D_R Q_0^{3/2} = \left(\frac{\eta}{S}\right)^{\frac{1}{2}}\ \frac{nq^3}{q'\ (1 + 2q^2)^{\frac{1}{2}}}\ \frac{\beta_0}{\rho}\ \frac{dP_{eq}}{d\rho}\left[1 - \frac{1}{q^2} + \frac{qq'}{\rho^3}\right.$$

$$\left. x \int_0^\rho \left(\frac{r^3}{q^2} - \frac{\beta_0}{\varepsilon^2}\ r^2\ \frac{dP_{eq}}{dr}\right) dr\right] \tag{21}$$

Inherent in the derivation of Eq. (19) is the assumption that the sound speed $\omega_s >> \omega$. Since $\omega_s = (\gamma\beta_0 P/2q^2)^{\frac{1}{2}}$ [normalised to τ_{HP}] we see that it is appropriate to compare the incompressible numerical results ($\gamma=\infty$) with the dispersion relation. Figure 1 compares the n=1 growth rate (ω) as a function of β_0 between the dispersion relation [Eq. (19)]

and the numerical incompressible results. There is good agreement between the dispersion relation and numerical results. In this case $P\alpha\psi^2$ is assumed, $S=5\times10^6$, $\eta=1$, and the cylindrical value for Δ' is used in the dispersion relation. The numerical calculations retain the poloidal harmonics m=0 to 4, with 450 mesh points. The small discrepancy between the dispersion relation and numerical results at β_0 = 0.1% in Fig. 1 may in part be due to the fact that Δ' is actually changing with β_0.

Examining the dispersion relation [Eq. (19)], the first term ($\alpha\omega^{5/4}$) represents the β=0 tearing mode while the second term ($\alpha D_R\omega^{-1/4}$) is responsible for the stabilisation effect from the favourable average curvature in the Tokamak ($D_R<0$). As S increases (and ω decreases) so the relative importance of the average curvature term increases. Figure 2 shows the trajectory of the growth rate in the complex ω-plane as S is increased for the same case as Fig. 1 at β_0 = 0.25%. Results are shown for the dispersion relation (a) and the incompressible code (b); the numbering on the curves is the S value. The trajectory for the numerical incompressible results can not be followed into the stable region ($\omega_I<0$) because the initial value method requires a growing solution. This type of overstable behaviour is characteristic of the 4th order differential equations which occur when sound waves interact with the resistive instability; such behaviour also occurs for the resistive ballooning mode [13,14]. The growth rates when the solution becomes overstable are usually very low (typically $\omega\sim\tau_R/10$ for the cases examined in this paper) and their experiment relevance is questionable.

Finally, it is worth remarking that this single rational surface case is somewhat pathological. The constraints on the q-profile mean that Δ' is relatively small (~ 2) and so we are forced to low β_0 in order to avoid being stabilised by the curvature terms (D_R). This in turn means that the sound speed is low and there is a marked difference between the incompressible and compressible (low γ) cases. In fact in the regime $\omega >> \omega_s$ it is difficult to achieve converged numerical results with the compressible code and we have not made an extensive survey of the effects of compressibility in this case. Apart from the effects of compressibility however the multiple rational surface cases at tight aspect ratio, have exactly the same qualitative behaviour as this large aspect ratio case.

4 JET Results

We shall now examine the stabilising effect of β_0 on tearing modes, for parameters consistent with JET equilibria. For these cases we take the inverse aspect ratio (relative to the horizontal minor radius) to be 0.39. At such tight aspect ratios and with multiple rational surfaces in the plasma there is strong coupling between the poloidal harmonics. Figure 3 shows a convergence study of the poloidal spectrum for a JET circular boundary equilibrium with $q=1.1(1+(\rho/0.506)^8)^{1/4}$, $\beta_0=0.5\%$, $S=10^5$, $n=1$, and $\eta=\langle 1/J_\xi \rangle$ (where $\langle\rangle$ denotes a flux surface average). The pressure profile is $P_{eq}\alpha\psi^2$ and will be so throughout this paper. The poloidal magnetic energy spectrum

$$E_{\psi mn} = \int \left(\left| \frac{\partial \psi_{mn}}{\partial \rho} \right|^2 + \left| \frac{1}{\rho} \frac{\partial \psi_{mn}}{\partial \theta} \right|^2 \right) d\tau \qquad (22)$$

and the growth rates, shown in Fig. 3, can be seen to be converged by 7 harmonics. Typically for n=1 calculations for JET, we include the poloidal modes m=-1 to 7 and use 200 radial mesh points. This radial resolution is quite adequate for $S\sim10^5$ (assuming $\eta = 1/\langle J_s \rangle$) but for $S>10^6$ we perform calculations for several meshes and use a quadratic extrapolation to zero mesh size.

Figure 4 shows the n=1 growth rate as a function of β_0 in the incompressible and compressible ($\gamma=5/3$) regimes. The flow in the $\xi=0$ plane is shown in Fig. 5 for this case at $\beta_0=2\%$. The circular boundary equilibria in this case have $q=1.34(1+(\rho/0.558)^8)^{1/4}$ and $\varepsilon=0.39$ (ie JET) with $S=10^5$ and $\eta=\langle 1/J_\xi \rangle$. This q-profile is particularly unstable to n=1 and n=2 tearing modes at $\beta=0$, and has been used extensively in disruption studies [15, 16]. Despite this a strong stabilising effect is evident in Fig. 4 as β_0 is raised. The $\gamma=\infty$ curve in Fig. 4 is from the incompressible code, although we have verified numerically that as $\gamma\to\infty$ the compressible results limit to this value. The compressible and incompressible results agree well except near $\beta=0$ where the regime $\omega_s \ll \omega$ occurs for the compressible case. The dispersion relation appropriate to this regime is

$$\Delta' = 2.12\ \omega^{5/4} \left(\frac{nq'}{q}\right)^{-1/2} \left(\frac{\eta}{S}\right)^{-3/4} \qquad (23)$$

This is the normal cylindrical result [2] and differs from the $\beta\to0$ limit of Eq. (19) in the omission of the $(1+2q^2)^{1/4}$ term of V_s/X_0. The $(1+2q^2)$ term is related to the compressional waves damping the tearing mode and so is absent when $\omega \gg \omega_s$. Thus we expect the $\beta = 0$ limit of the incompressible case ($\gamma=\infty$) to differ from the compressible

result ($\gamma\neq\infty$) by $(1+2q^2)^{1/5}=1.55$. Even though this case (Fig. 4) is tight aspect ratio and has several resonant surfaces the ratio of the compressible to incompressible $\beta=0$ growth rates (=1.76) is still near the analytic single helicity ratio for the m=2 mode of 1.55.

The S value (10^5) used in Fig. 4 is much lower than that in the JET experiment, which is typically $S\approx10^7$ to 10^8. If we increase S for the same case as Fig. 4 at $\beta_0=2\%$, then the importance of the average curvature terms within the layer increases and the growth rate eventually decays much faster than the tearing mode scaling ($\alpha S^{-3/5}$) and becomes overstable (Fig. 6). For values of S consistent with JET the dispersion relation shows that the mode is completely stable (we are unable to confirm this numerically because the initial value method requires a growing solution). For the computation shown in Fig. 6 we have used the incompressible code, although because $\omega<<\omega_s$ we find that the compressible code ($\gamma=5/3$) gives almost identical results. From Eq. (19) we see that a scaling of the growth rate as $S^{-3/5}$ indicates that the curvature terms are not playing an important role in determining the growth rate. Thus since in Fig. 6 the growth rate scales as $S^{-3/5}$ for $S=10^5$ we may conclude that the stabilisation for $\beta_0<2\%$ in Fig. 4 is not due to the curvature terms. Instead it is caused by changes in the equilibrium profiles and poloidal mode couplings as β_0 is increased.

We now examine a circular boundary case which is less unstable to tearing modes at $\beta_0=0$, $q=1.1(1+(\rho/0.506)^8)^{1/4}$; in this case the n=1 tearing mode growth rates are significantly reduced by $\beta_0=1\%$ at $S=10^5$ (Fig. 7). There are three curves in Fig. 7, two of which are the compressible ($\gamma=5/3$) and incompressible results with the q-profile as a

function of ρ held constant as β_0 is raised. The remaining curve corresponds to conserving the $FdF/d\psi$ profile as β_0 is raised (with q at the axis =1.1) and is for the incompressible limit. By raising β_0 at constant q we are implicitly changing the current profile which itself affects the growth rate. The difference between the q-constant and $FdF/d\psi$ constant results (in Fig. 7) indicates that the effects of the finite-β modifications to the profile are relatively small. The ratio of the compressible to incompressible results at β=0% is 1.72 here, which again is in reasonable agreement with the analytic prediction. Since however the regime $\omega >> \omega_s$ is of little interest for present day Tokamaks we have not bothered to examine the region near β=0 in detail. For this case (Fig. 7) we have so far considered $S=10^5$, by raising this to higher values the instabilities are further stabilised. Figure 8 shows how the incompressible growth rates vary with S for β_0=0, 0.5 and 1% (q-constant). At large S ($>10^6$) the β_0=0 growth rate asymptotes to the tearing scaling ($S^{-3/5}$) while the β_0=0.5 and 1% cases decay much faster than this and become overstable. The compressible (γ=5/3) results show very similar behaviour as S is increased. The trajectories in the complex ω-plane as S is increased at β_0=1% are compared for the γ=5/3 and $\gamma=\infty$ (incompressible) cases in Fig. 9.

For this profile $[q=1.1(1+(\rho/0.506)^8)^{1/4}$, ε=0.39] the ideal ballooning threshold is β_0=6% (Fig. 10) and hence there is a significant region of complete stability to the ideal ballooning mode and n=1 tearing mode (β_0=1.5 to 6% at $S=10^5$). The critical β_0 for ideal ballooning scales as ε [17], whilst at constant S the average curvature stabilisation terms are independent of ε; hence the region of stability to both the n=1 tearing mode and ideal ballooning mode shrinks as the aspect ratio is increased (at constant S). Figure 10

shows the ideal ballooning ($n=\infty$) growth rates as a function of β_0 for several γ value with $\varepsilon=0.2$ and 0.39, and $q=1.1(1+\rho/0.506)^8)^{1/4}$. The ballooning growth rates are quite sensitive to γ but the marginal points are independent of γ. The difference in the critical β_0 is in good agreement with the inverse aspect ratio scaling predicted by Troyon/Sykes [17,18]. It should be noted for the tearing modes that by holding S constant as we change the aspect ratio, we are imposing the requirement that n and T be varied to keep $a^2T^{3/2}/(Rn^{\frac{1}{2}})$ constant. If instead we make the more physical assumption of $n\alpha T$ (and allow S to vary) then the critical β_0 which must be exceeded to stabilise the tearing mode scales as $(R/a^2)^{1/3}$. Hence with this assumption the region of stability to the n=1 tearing mode and ideal ballooning mode shrinks even more rapidly, since the critical β for stability to the tearing mode now increases as the aspect ratio is raised.

Raising the aspect ratio also effects the stability of the ideal n=1 modes. For the free boundary n=1 mode the critical-β for instability scales, like the ideal ballooning mode, as the inverse aspect ratio [17]. The global nature of the free boundary n=1 mode means that it is sensitive to the position of the conducting wall; placing it at the plasma boundary has a strong stabilising influence on the mode. A detailed parameter study of the fixed boundary internal kink has been given by Manickam [19]. His results show that at high-β ($\varepsilon\beta_p \sim 0.8$) the n=1 internal kink remains unstable for a central $q_0 > 1$. This effect is particularly pronounced for large aspect ratio, peaked pressure profiles, and q-profiles with low shear near the axis. At still higher β ($\varepsilon\beta_p > 1.2$ for $q_a/q_0 = 4$) the internal kink is stabilised (for all q_0) as it enters the second region of stability.

For the profile $q=1.1(1+(\rho/0.506)^8)^{1/4}$ at aspect ratio 5 the n=1 tearing mode ($S=10^5$) is not completely stabilised as β_0 is raised (Fig. 11). This is in contrast to the JET aspect ratio case (Fig. 7) which is stabilised by β_0 = 1.5%. The increase in growth rate for $\beta_0>2\%$ in Fig. 11 is associated with the mode becoming ideally unstable. By β_0 = 5% ($\varepsilon\beta_p=0.7$) the growth rate of the mode is almost independent of S (Fig. 12); indicating an ideal mode. For higher β the growth rate of the $q_0=1.1$ case decreases and becomes completely stable for $\varepsilon\beta_p>1.2$ as the ideal mode enters its second region of stability. At these high-β's the curvature stabilisation is very strong and the tearing mode is stable. The behaviour of the ideal mode in this case is in good agreement with the results of Ref. [19]. Also shown in Fig. 11 is the behaviour of the n=1 growth rate with β_0 for the profile $q=1.34(1+(\rho/0.558)^8)^{1/4}$. In this case, because of the higher q, the mode does not become ideally unstable, and the tearing mode is stabilised by $\beta_0=5\%$ at $S=10^5$. For the $q_0=1.1$ case in Fig. 11 it is possible to achieve a region of stability to the tearing mode, and ideal ballooning and n=1 modes, by increasing S. Figure 12 indicates at $\beta_0=2\%$ that the n=1 tearing mode is stabilised by the curvature terms at high S.

For all the JET cases presented so far in this section we have used broad current profiles. To study the effect of more peaked profiles we use the parameterisation $q=1.1(1+[(4.3/1.1)^{\lambda}-1]\rho^{2\lambda})^{1/\lambda}$. By varying λ we can go from flat ($\lambda=4$), to rounded ($\lambda=2$), to peaked ($\lambda=1$) current profiles [20]. Figure 13 shows how the n=1 growth rates vary with λ for $\beta_0=0$ and 0.5%, with $S=10^5$ and $\varepsilon=0.39$. The reduction in growth rate as λ decreases is mainly attributable to the reduction in shear and $\eta(=1/\langle J_{\xi}\rangle)$ at the q=2 surface. By $\lambda=1.5$ the $\beta_0=0.5\%$ case is

stable. Thus the n=1 tearing mode is stabilised at lower β_0 (or S) for the more peaked profiles.

Finally we examine the effects of β_0 on the n=2 (predominantly m=3 at β_0=0%) tearing mode. This mode is harder to destabilise than the m=2, n=1 mode and requires broad current profiles; we use the relatively unstable q-profile used for Fig. 4 $[q=1.34(1+(\rho/0.558)^8)^{1/4}]$. Figure 14 shows that incompressible growth rate as a function of β_0 for the n=2 mode in this case; here $S=10^5$, $\eta=<1/J_\xi>$, and $\varepsilon=0.39$. At this value of S there is no region of stability to the n=2 tearing mode, although the n=1 mode is stable by β_0=4% (Fig. 4). For this profile the ideal ballooning threshold is β_0=5.5%. At high-β the magnetic energy spectrum becomes very broad and the n=2 mode has a strong ballooning character. Figure 15 compares the magnetic energy in the dominant poloidal harmonics between the β_0=0% and 8% cases shown in Fig. 14. At the higher β the spectrum is much broader and actually peaks at m=4.

For the n=2 ideal mode the instability is more radially localised that the n=1 mode and the conducting wall position has less effect. Figure 16 shows the growth rate of the ideal n=1 and n=2 modes as a function of β_p computed with the ERATO stability code [21]. The equilibria in this case have $dP/d\psi = -(1 + a)\,\psi$, $FdF/d\psi = a\psi + 0.63\,a\psi^3$, $\varepsilon = 0.39$ and $q_0 = 1.2$; where 'a' is varied to alter the β_p. Results are shown in Fig. 16 for the wall infinitely far from the plasma and at the plasma surface. For the n=1 mode placing the wall at the plasma surface stabilises it in this case, whereas the more localised n=2 mode remains unstable for all wall positions. Results are also shown from FAR in Fig. 16; these are in reasonable agreement

the wall on plasma ERATO results. Figure 17 shows the velocity flow in the ξ=0 plane from the FAR code at β_p=2.2; the very strong ballooning character of the mode is evident. The strong ballooning character and relatively localised nature of the fixed boundary ideal n=2 mode mean that careful convergence studies are necessary. With ERATO we have used several computational grids (the finest being 90 radial intervals and 60 poloidal intervals) and then quadratic extrapolation to a zero mesh interval. With the FAR code we have used 120 radial grid points and the poloidal spectrum m=-2 to 11 (which is the limit imposed by computer memory). At the highest-β's (β_ρ>2.3) using slightly reduced poloidal spectrums indicates that the FAR growth rates are not fully converged for these very broad spectrum n=2 ballooning type modes; this may in part account for the discrepancy between the FAR and ERATO results.

Thus the failure of the n=2 mode to be completely stabilised with increasing β_0 (Fig. 14) arises because the n=2 fixed boundary ideal mode is destabilised before the tearing mode is stabilised (S=10^5). At higher S the curvature terms (D_R) will be more important and stabilise the tearing mode before the ideal n=2 threshold is exceeded. Figure 18 shows the S dependence of the n=2 growth rate for the same case as Fig. 13 at β_0=2%, and indicates that by raising S to large enough values then n=2 tearing can be completely stabilised.

For the n=2 mode we have only shown results from the incompressible FAR code. This is because the very broad spectrums of the n=2 mode require us to retain many poloidal harmonics to obtain numerically converged results. Unfortunately because of computer memory limitations we are unable to use so many modes in our

compressible calculations. Comparison of calculations with reduced spectrums (m=1 to 7) do however indicate that the effects of compressiblity on the n=2 growth rates are not too great (~10%).

5. Conclusions and Discussion

The finite-β properties of the tearing mode in the Tokamak have been studied computationally. A code has been developed which solves the linear compressible resistive MHD equations in toroidal geometry with no ordering assumptions. The computations confirm the analytic results of Glasser et al [1]; there is a strong stabilising effect as β is raised which results from the favourable average curvature terms ($D_R<0$), within the resistive layer. The importance of these stabilising average curvature terms increases as S (ie conductivity temperature) is raised. At large S the tearing mode growth becomes overstable and as S is raised still further the mode is stabilised ($\omega_I<0$). Examining the scaling of the critical β for tearing mode stability [Eq. (3)] shows that this tearing mode stabilisation will be particularly pronounced at high temperature and low aspect ratio. To confirm this we examine the finite-β behaviour of tearing modes for equilibria with the inverse aspect ratio ε=0.39, which is consistent with JET. For q-profiles which are moderately unstable at β = 0 ($\Delta' \sim$ 5), we find that the n=1 tearing modes can be completely stabilised by β_0=1.5% (at S=10^5). Since for these cases the critical β for ideal ballooning is 6%, there is considerable region of complete stability to the n=1 tearing mode and ideal ballooning mode (β_0=1.5-6%). Raising the aspect ratio causes the critical β for ideal ballooning to decrease inversely. Also increasing the aspect ratio with the assumption $n\alpha T$ means that critical β for stability to the tearing mode increases as

$(R/a^2)^{1/3}$. Thus as the aspect ratio is increased the range of β over which the n=1 tearing and ideal ballooning modes are stable shrinks and eventually disappears.

Since generally the sound waves propagate faster than the tearing mode growth time ($\omega_s >> \omega$) the compressible ($\gamma=5/3$) results differ very little from the incompressible results. In the region near $\beta=0$ where the sound speed is low ($\omega_s \to 0$ as $\beta_0 \to 0$) the $\gamma=5/3$ and $\gamma=\infty$ results do differ markedly; this behaviour however appears to be of little relevance for present day Tokamaks.

For the n=2 tearing mode it is harder to achieve complete stability. This is because at high-β the n=2 fixed boundary ideal mode is destabilised. It should be noted however that the n=2 tearing mode is intrinsically harder to destabilise than the n=1 mode and requires broad current profiles.

In this paper we have only considered equilibria with circular boundaries. Elsewhere we have considered the effects of D-shaping, at JET aspect ratio, on the tearing mode [22]. The effects of increasing the D-shaping were shown to be strongly dependent on whether $q(\rho)$ or $FdF/d\psi$ was held constant as the shape was changed. For modest levels of shaping ($b/a \approx 1.4$) there was no clear effect on the finite-β tearing mode stability. It is worth noting here however, that the shaping does have a marked influence at high-β on the stability of low n ideal modes and $n=\infty$ ideal ballooning modes [23, 19]. Shaping will thus affect the behaviour of the n=2 and large aspect ratio n=1 modes in the regimes at high-β where they become ideally unstable. It will also alter the range in β over which the n=1 tearing mode and ideal ballooning mode

are stable, by increasing (or decreasing) the ideal ballooning β-limit.

Finally we note that linearly the average curvature stabilising effect relies on the properties of the resistive MHD equations within the tearing layer and thus further refinements to the theory (Finite Larmor Radius terms, Diamagnetic effects etc) may be important. Nonlinearly however, the curvature terms play an important role in determining the island growth rate [24], and so the results in this paper may be of relevance in situations where the linear resistive MHD equations appear inapplicable.

Acknowledgement

We are indebted to the Oak Ridge MHD group for providing us with a copy of the FAR code and the associated equilibrium code. We should also like to thank the Lausanne group for providing us with a copy of ERATO. This work was performed under a task agreement between the JET Joint Undertaking and Culham Laboratory.

References

[1] A H Glasser, J M Greene, J L Johnson Phys Fl 18 (75) 875.

[2] B Coppi, J M Greene, J L Johnson, Nucl Fus 6 (66) 101.

[3] A H Glasser, J M Greene, J L Johnson, Phys Fl 19 (76) 567.

[4] R J Hastie, A Sykes, M Turner, J A Wesson, Nucl Fus 17 (77) 515.

[5] L A Charlton, J A Holmes, H R Hicks, V E Lynch, B A Carreras, J Comp Phys 63 (86) 107.

[6] H R Strauss, Phys Fl 20 (77) 1354.

[7] R Izzo, D A Monticello, W Park, J Manickam, H R Strauss, R Grimm, K McGuire, Phys Fl 26 (83) 2240.

[8] B A Carreras, H R Hicks, D K Lee, Phys Fl 24 (81) 66.

[9] R Izzo, D A Monticello, J DeLucia, W Park, C M Ryu, Phys Fl 28 (85) 903.

[10] R L Dewar, J Manickam, R D Grimm, M S Chance, Princeton Plasma Phys Lab Report PPPL-1663.

[11] V E Lynch, B A Carreras, H R Hicks, J A Holmes, L Garcia, Com Phys Comm 24 (81) 465.

[12] A Jennings, 'Matrix methods for scientists and Engineers', Willey 1977, p 291.

[13] A H Glasser, M S Chance, R L Dewar, Proc of the 9th European Conf. on Controlled Fusion (1979), paper A3.1.

[14] T C Hender, B A Carreras, W A Cooper, J A Holmes, P H Diamond, P L Similon, Phys Fl 27 (84) 1439.

[15] B A Carreras, H R Hicks, J A Holmes, B V Waddell, Phys Fl 23 (80) 1811.

[16] W Park, D A Monticello, R B White, K McGuire, M Reush, Proc of 3-D MHD workshop Oak Ridge (1981).

[17] F Troyon, R Gruber, H Saurenmann, S Sementasato, S Succi, Plasma Phys 26 (84) 209.

[18] A Sykes, M F Turner, S Patel, Proc 11 European Conf on Cont Fusion Aachen (1983), paper B23.

[19] J Manickam, Nucl Fus 24 (84) 595.

[20] H P Furth, P H Rutherford, H Selberg, Phys Fl 16 (73) 1054.

[21] R Gruber, F Troyon, D Berger, L C Bernard, S Rousett, R Schreiber, W Kerner, W Schneider, K V Robers, Comp Phys Comm 21 (83) 323.

[22] T C Hender, R J Hastie, D C Robinson, Proc the 13th European Conf on Cont Fusion, Schliersee (1986).

[23] K Yamazaki, T Amano, H Naitou, Y Hamada, M Azzumi, Nucl Fus 25 (83) 1543.

[24] M Kotschenreuther, R D Hazeltine, P H Morrison, Phys Fl 28 (85) 294.

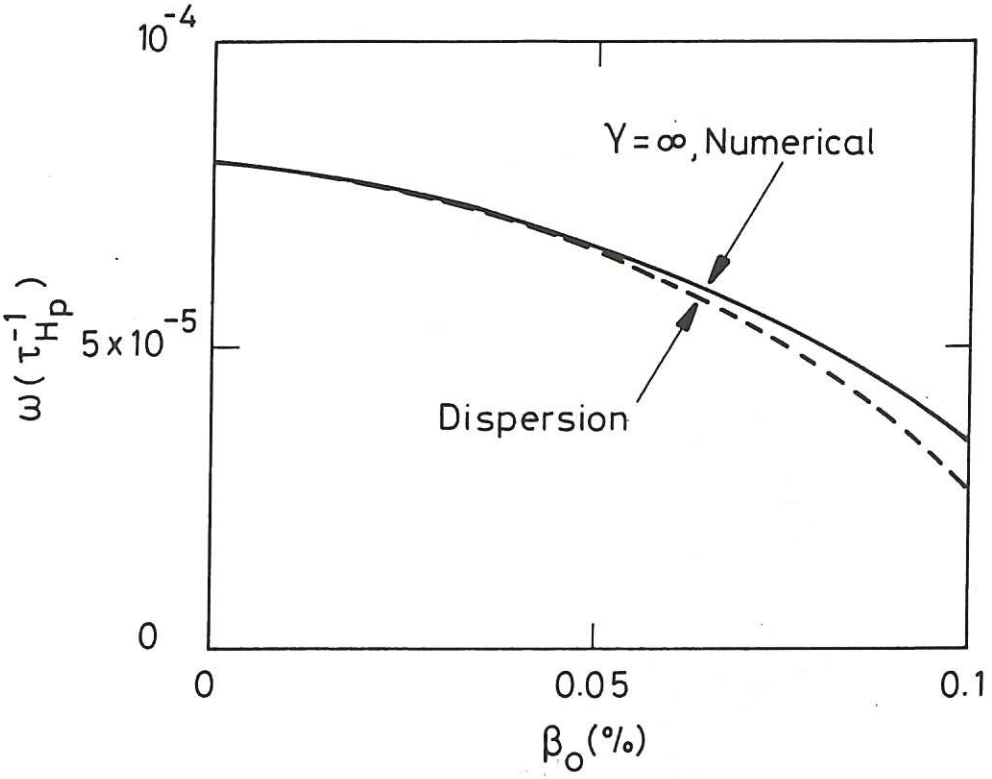

Fig. 1 Growth rate (ω) as a function of central beta (β_0) comparing the dispersion relation [Eq. (19)] and incompressible numerical results, n=1, S=5x10^6, and ε=0.05.

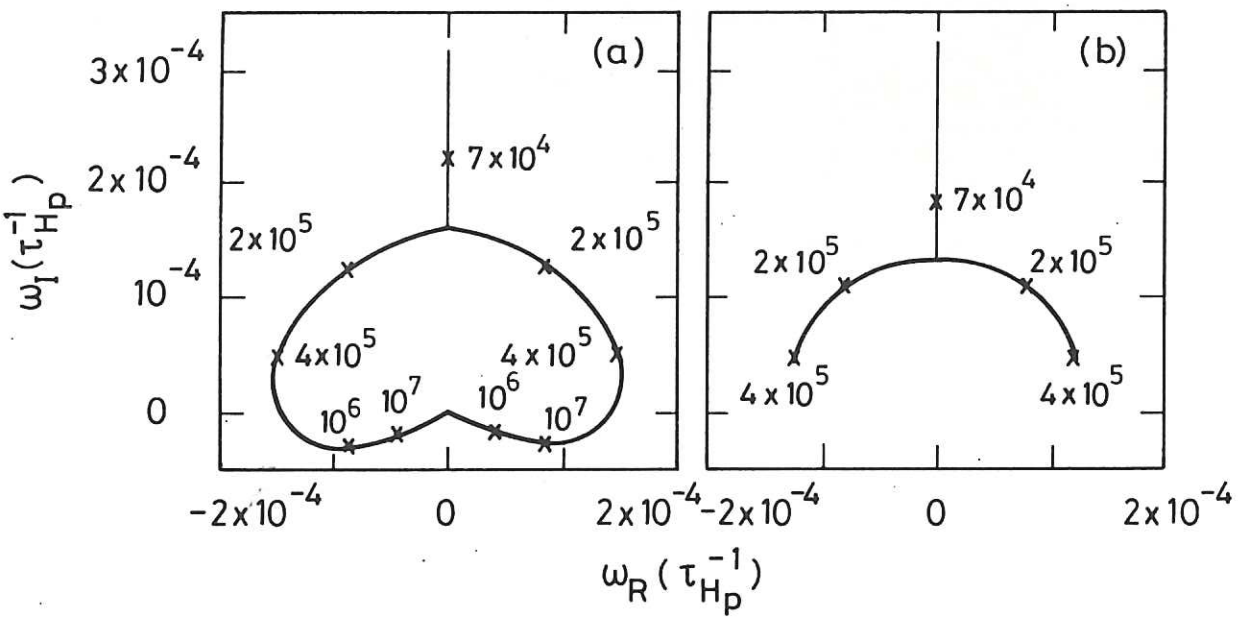

Fig. 2 Growth rate as a function of S for, (a) dispersion relation, and (b) numerical ($\gamma=\infty$) computation. The labels are S values, β_0=0.25%, and all other parameters as Fig. 1.

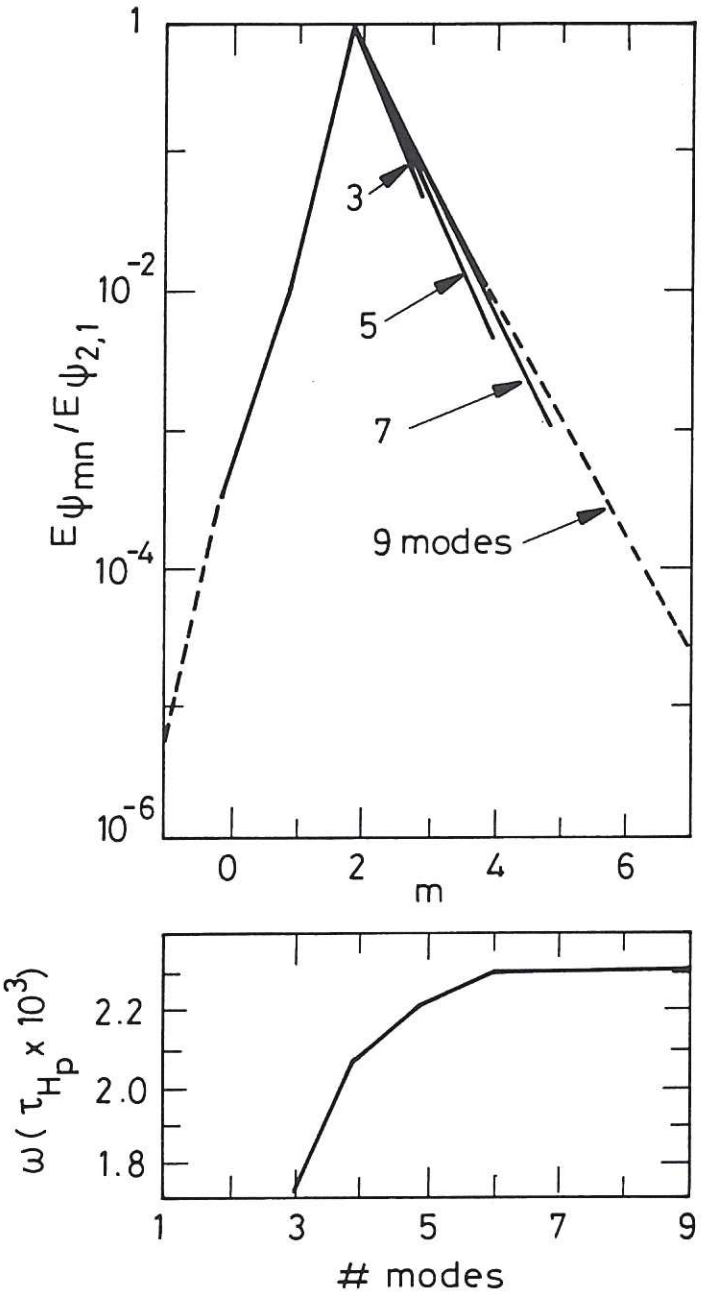

Fig. 3 Energy spectrum and growth rates showing convergence as the number of harmonics are increased, $q=1.1(1+\rho/0.506)^{8^{1/4}}$, $S=10^5$, $n=1$, $\varepsilon=0.39$.

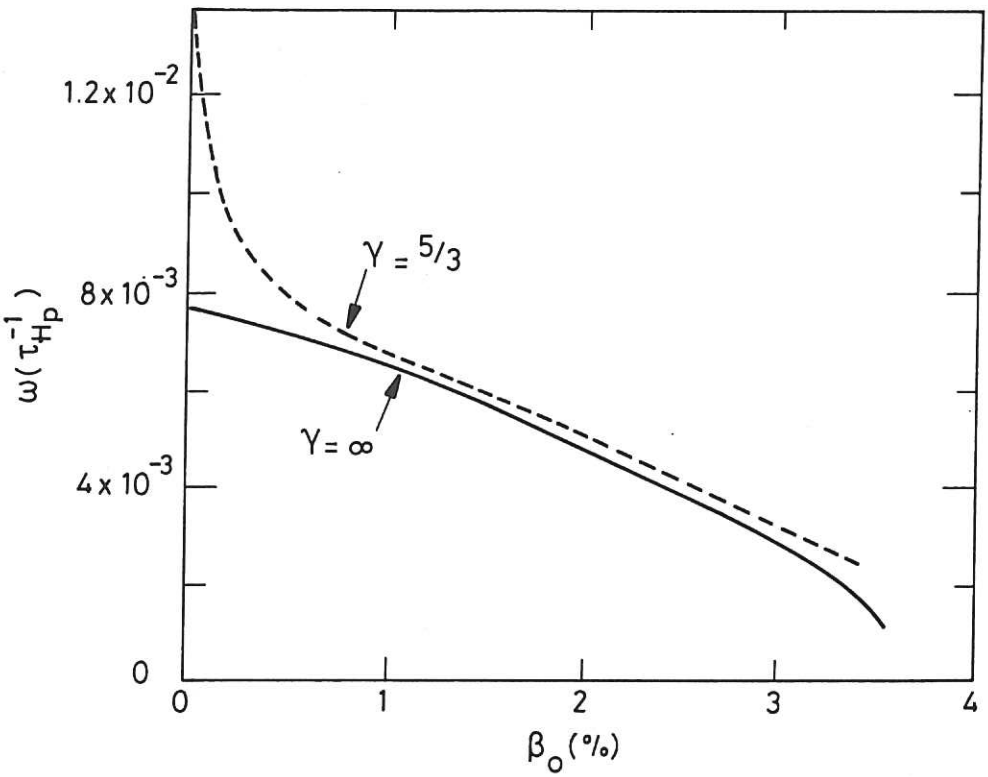

Fig. 4 Growth rate (ω)v β_0 for relatively unstable q [$=1.34\ (1 + (\rho/0.558)^8)^{1/4}$], $S=10^5$, $n=1$, $\varepsilon=0.39$.

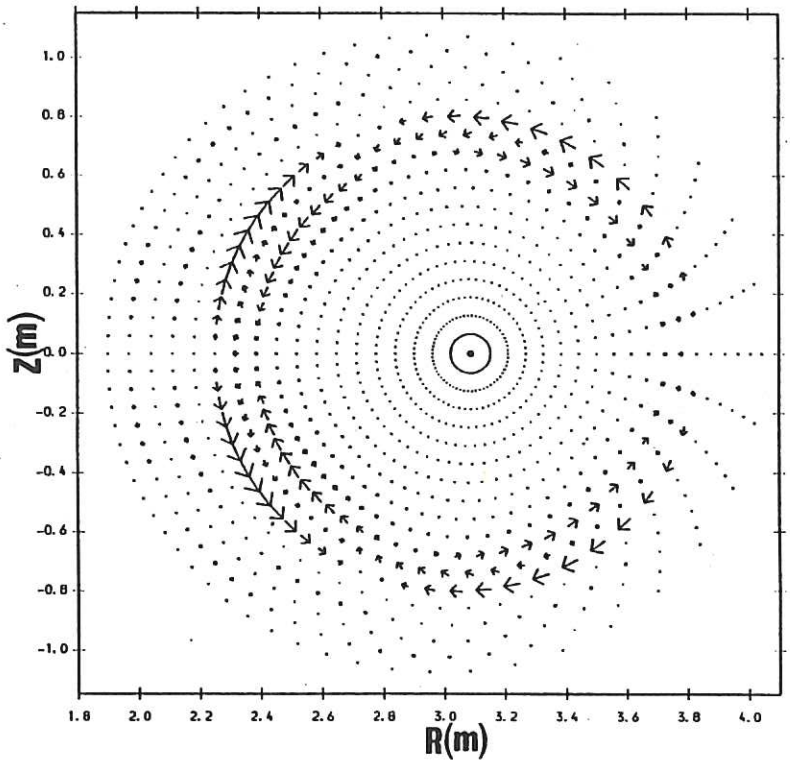

Fig. 5 Velocity flow in $\xi=0$ plane for the same case as Fig. 4 at $\beta_0=2\%$.

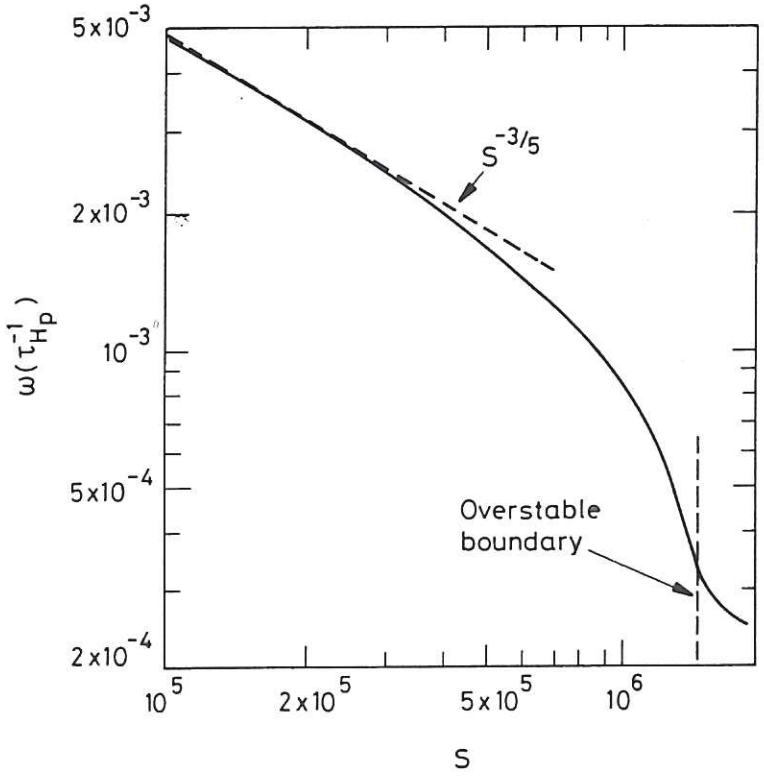

Fig. 6 Growth rate v S for same case as Fig. 4 at β_0=2%. Growth rates are overstable to the right of the indicated boundary.

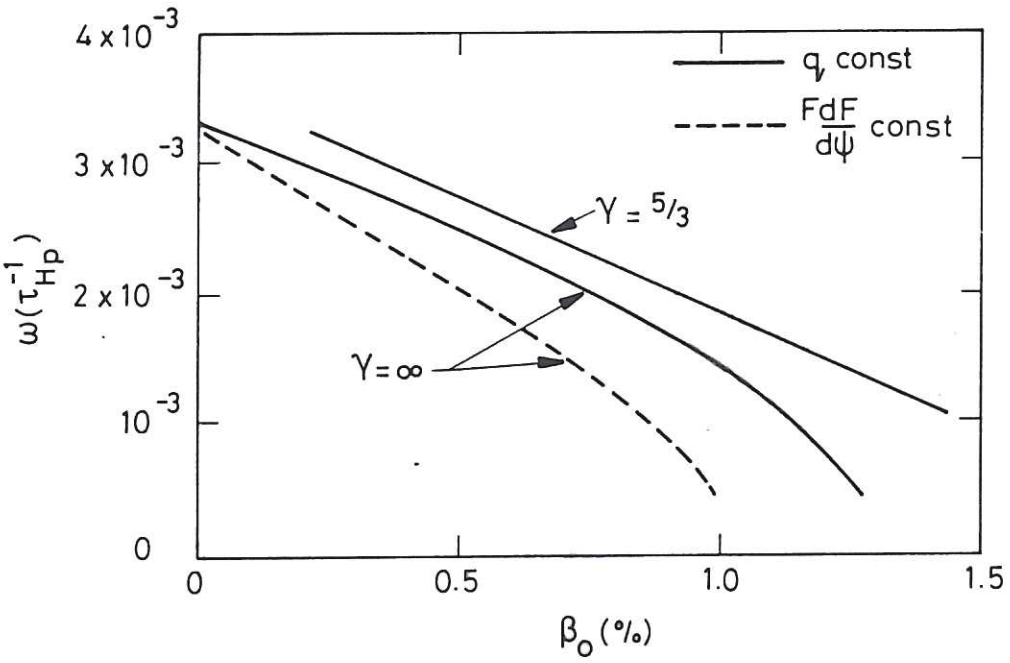

Fig. 7 Growth rate (ω) V β_0 for moderately unstable q $[=1.1(1+(\rho/0.506)^8)^{1/4}]$ with $S=10^5$, n=1, ε=0.39.

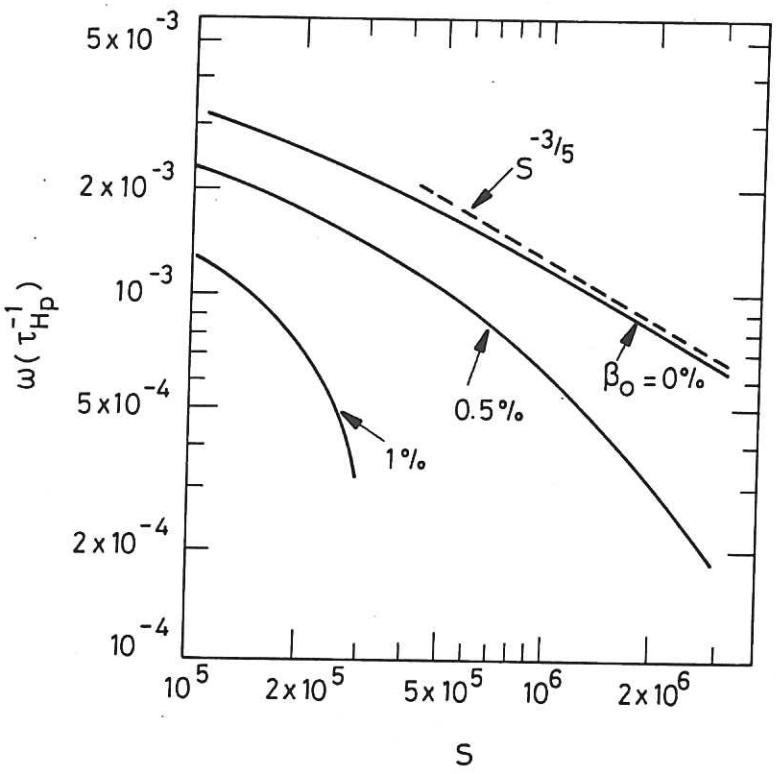

Fig. 8 Growth rate (ω) as a function of S for same case as Fig. 7 at β_0=0, 0.5 and 1%. For β_0=0.5 and 1% the growth rate is just overstable at the highest S values shown.

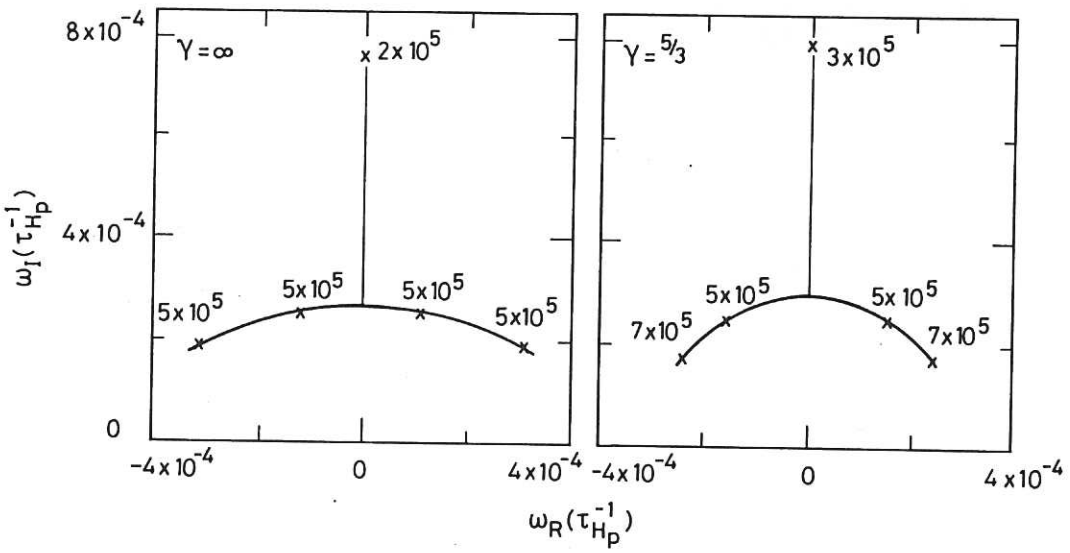

Fig. 9 Trajectories in the complex ω-plane as S is increased for compressible and incompressible cases (same case as Fig. 7, β_0=1.0%).

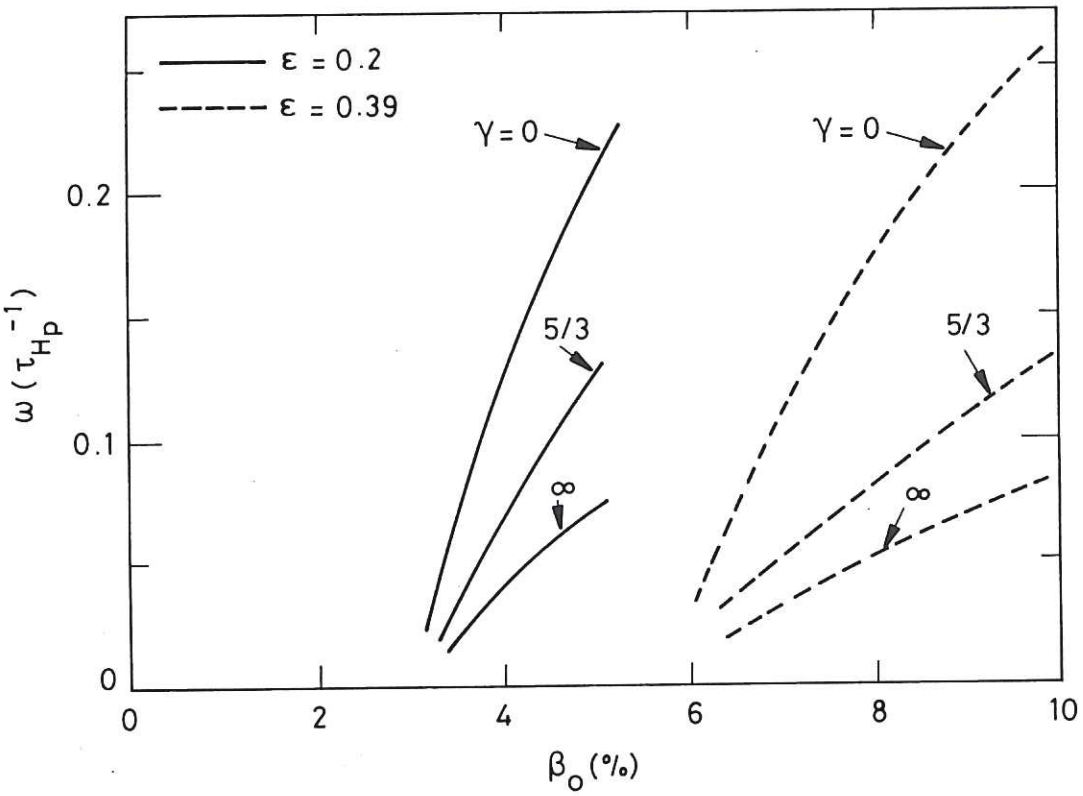

Fig. 10 Ideal ballooning growth rates for various specific heat ratios (γ) at ε=0.2 and 0.39 [$q=1.1(1+(\rho/0.506)^8)^{1/4}$].

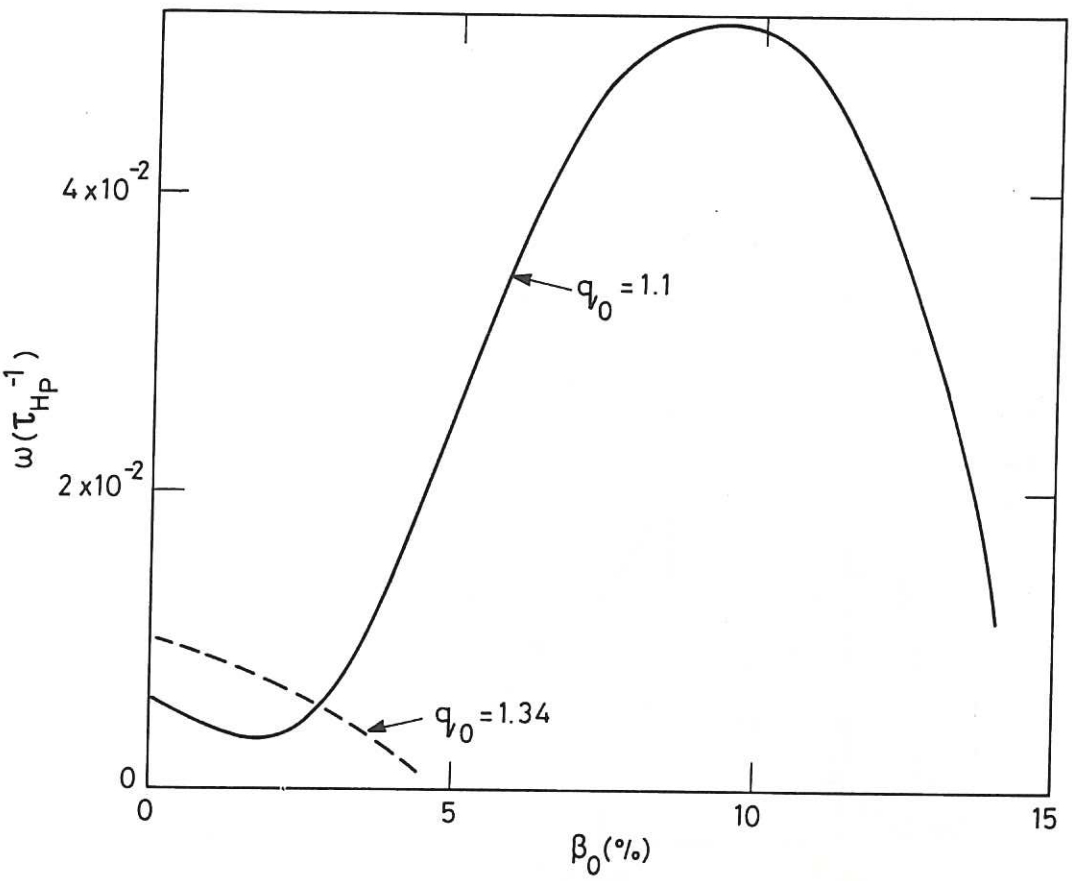

Fig. 11 Growth rate (ω) v β_0 for $q=1.1(1+(\rho/0.506)^8)^{1/4}$ and $q=1.34(1+(\rho/0.558)^8)^{1/4}$ at $\varepsilon=0.2$, $n=1$, $S=10^5$.

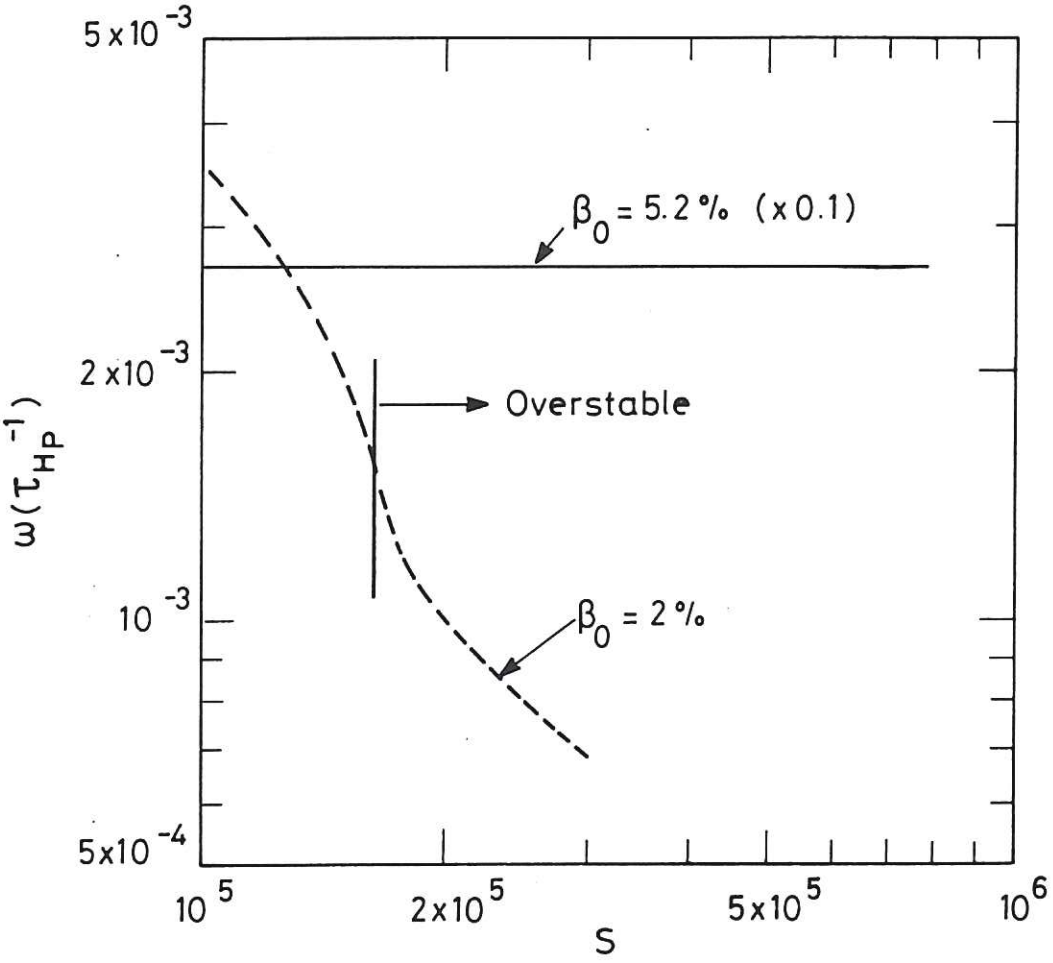

Fig. 12 Behaviour of growth rate with S for same case as Fig. 11 at β_0=2% and 5.2%. (The growth rate of the β_0=5.2% case is reduced by a factor of 10).

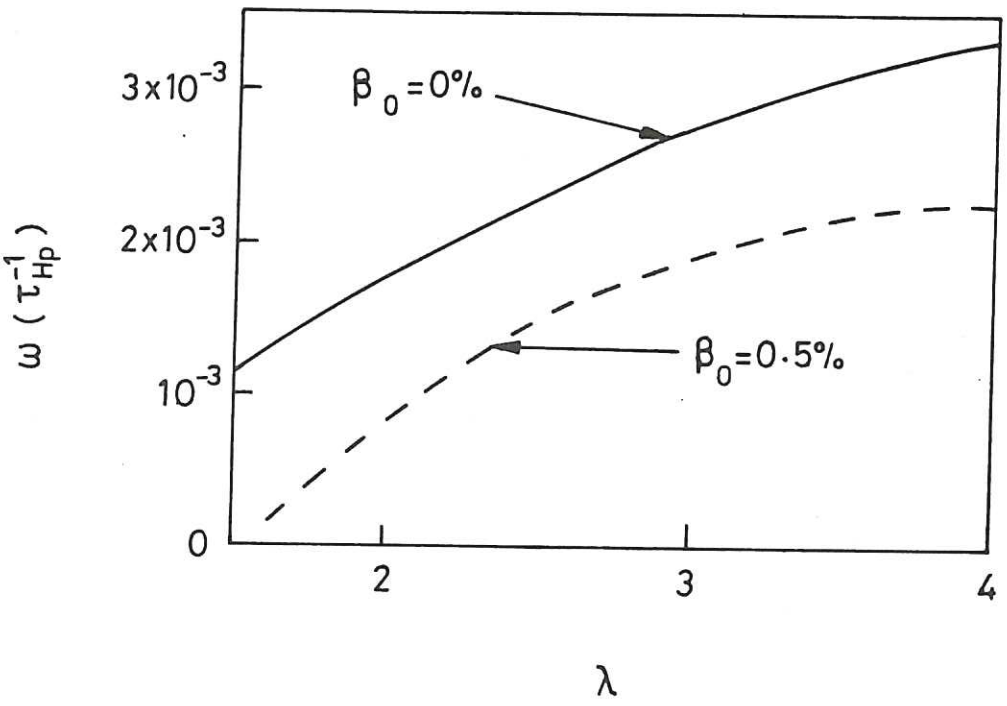

Fig. 13 n=1 growth rate v λ for $q=1.1(1+[(4.3/1.1)^{\lambda}-1]\rho^{2\lambda})^{1/\lambda}$ at $S=10^5$.

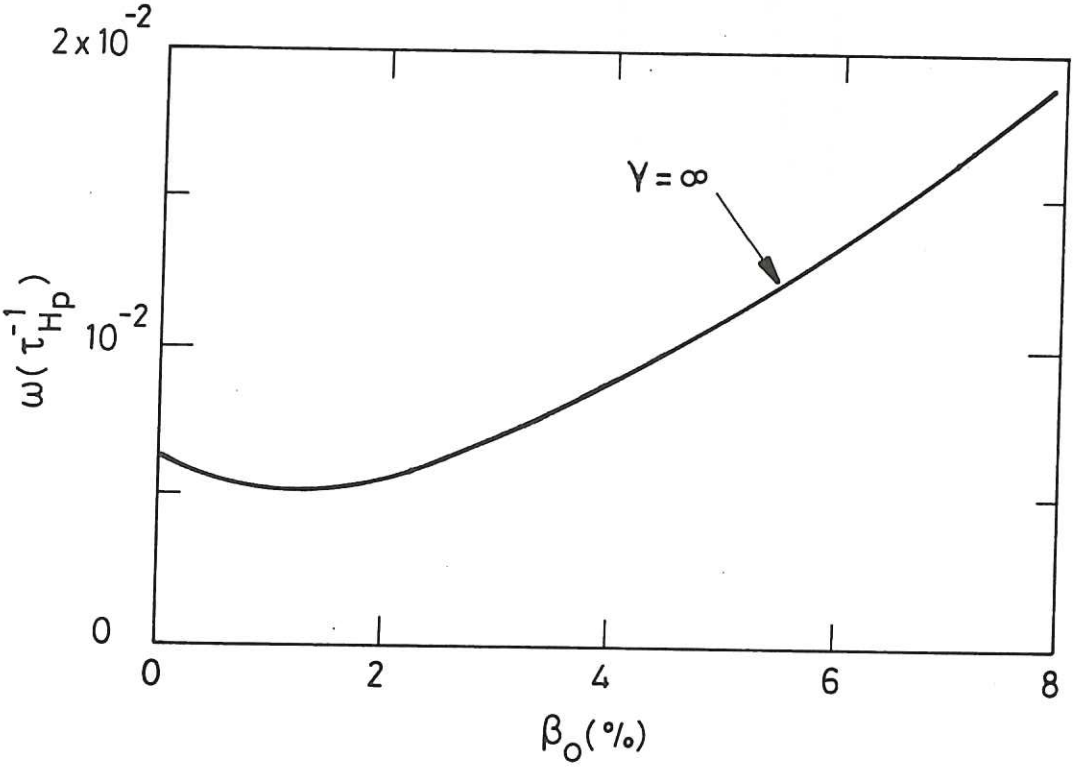

Fig. 14 n=2 growth rate v β_0 for the same case as Fig. 4.

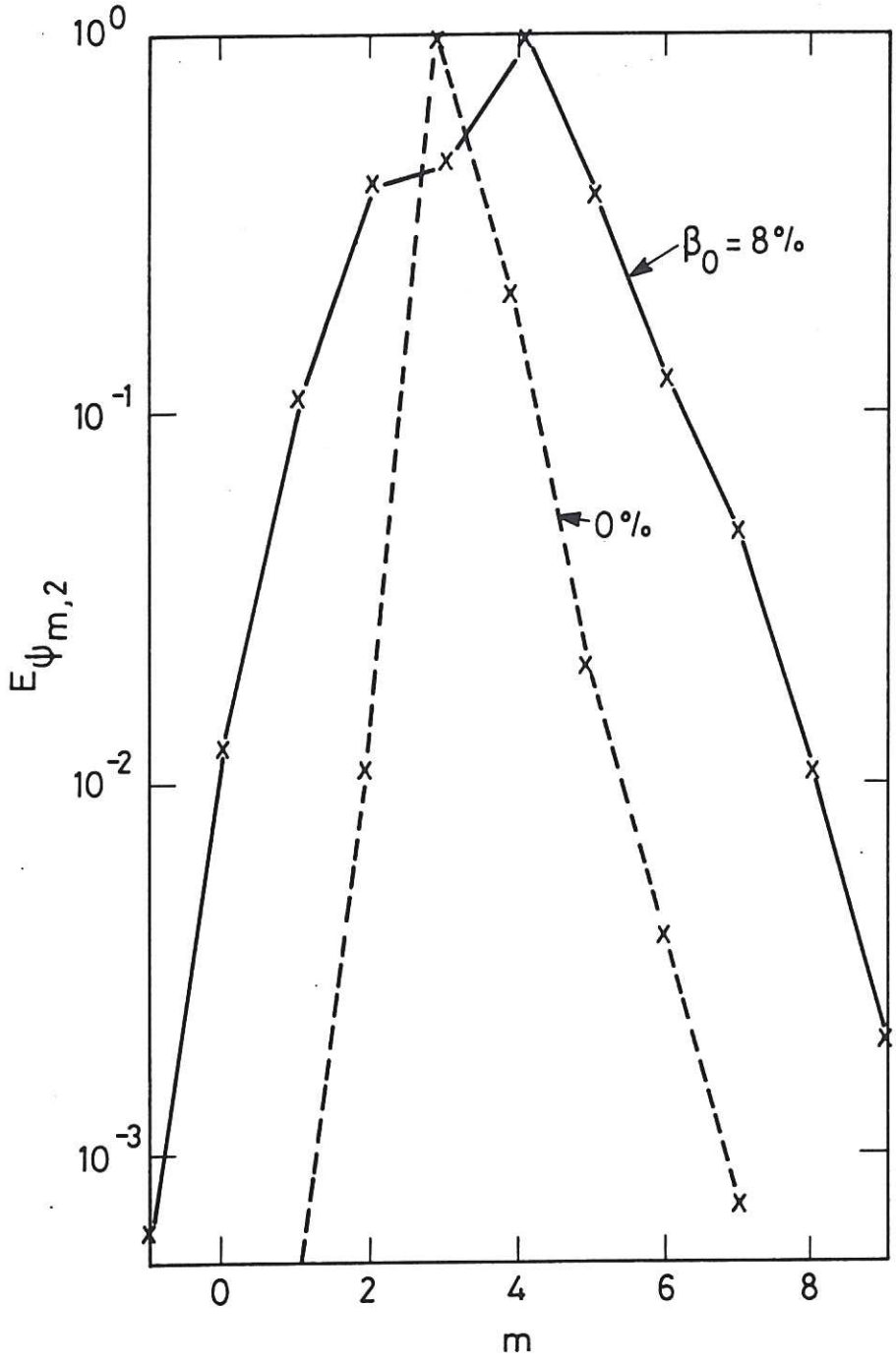

Fig. 15 Energy spectrum at β_0=0% and 8% for the same case as Fig. 14.

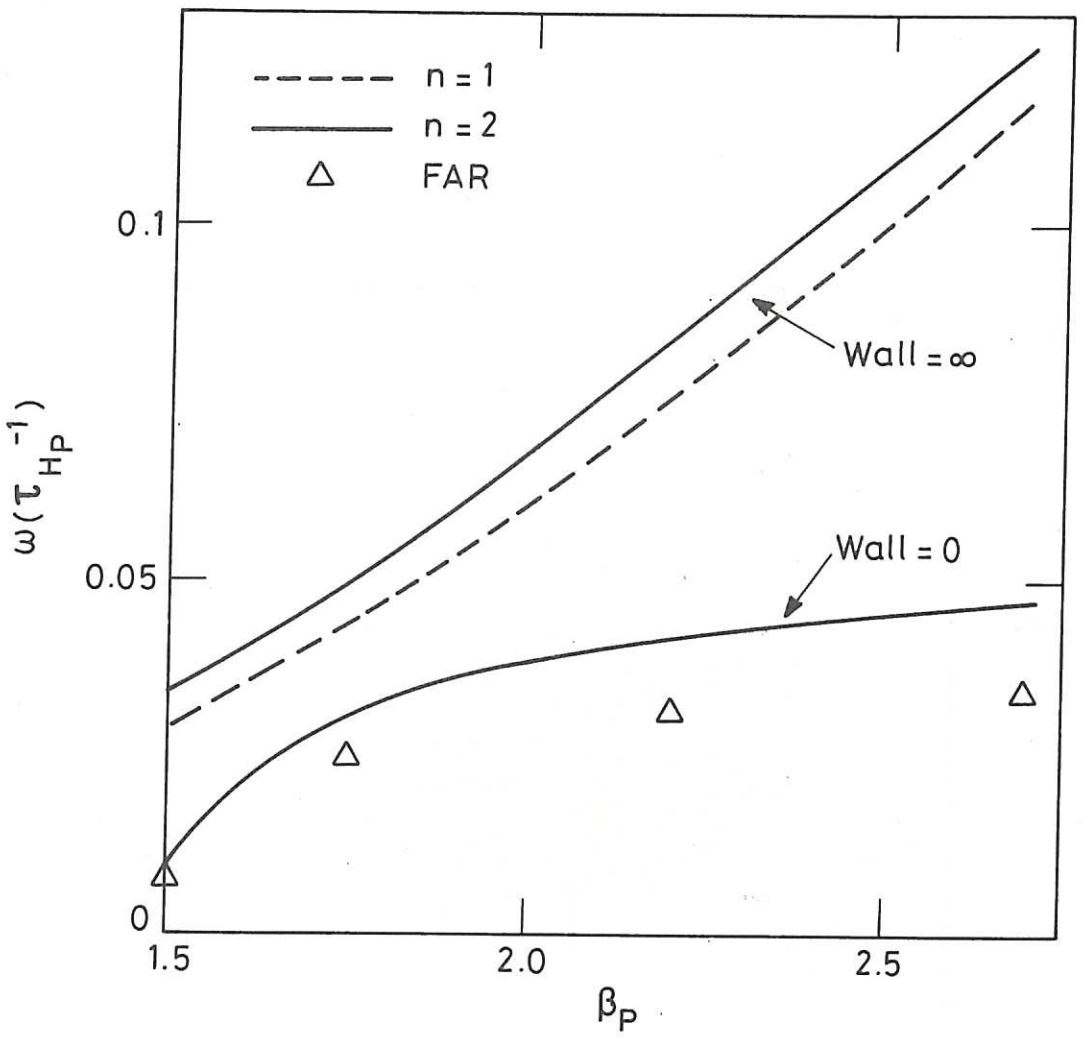

Fig. 16 Growth rate of the n=1 and n=2 ideal modes with the wall at the plasma surface (wall=0) and infinitely far from the plasma.

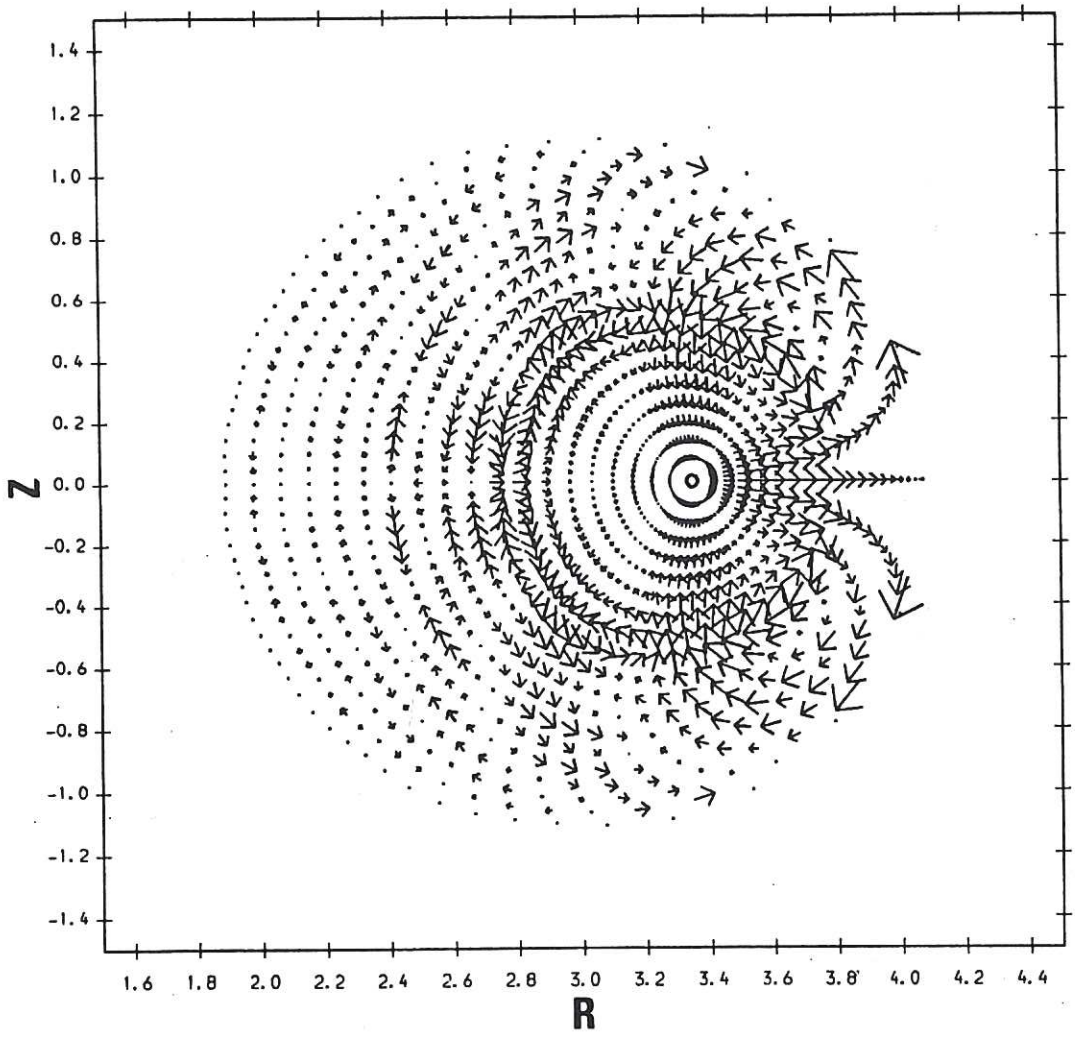

Fig. 17 Velocity flow in ξ=0 plane corresponding to β_p=2.2 FAR results in Fig. 16.

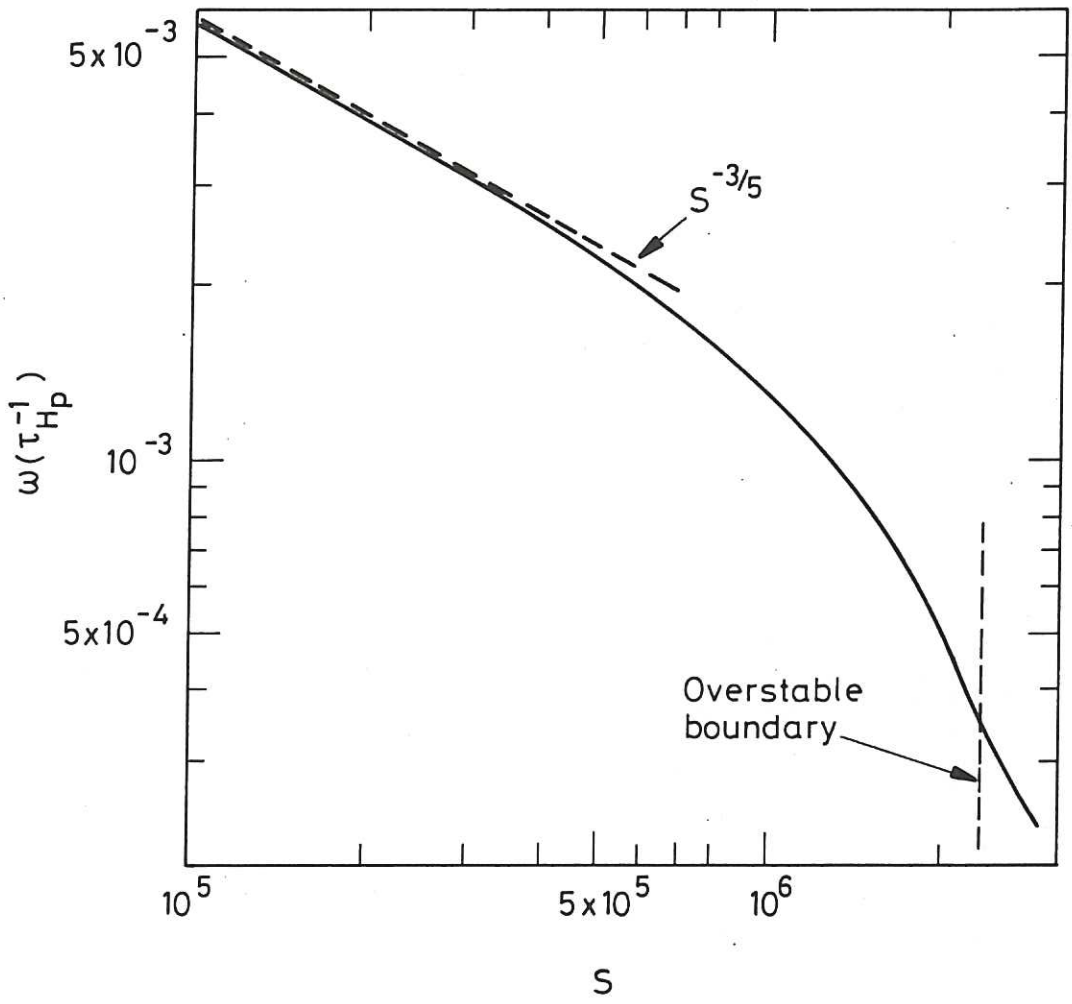

Fig. 18 Decay of n=2 growth rate with S for same case as Fig. 14, β_0=2%.